# Cavitation Damage Morphology of the Centrifugally Cast Heat-resistant Alloy – HP40 Nb

**Milica TIMOTIJEVIĆ [1], Olivera ERIĆ CEKIĆ [1, 2] *, Petar JANJATOVIĆ [3], Marina DOJČINOVIĆ [4], Dragan RAJNOVIĆ [3]**

[1] *Faculty of Mechanical and Civil Engineering in Kraljevo, University of Kragujevac, Dositejeva 19, 36000 Kraljevo, Serbia*
[2] *Innovation Center of Mechanical Engineering Faculty, University of Belgrade, Kraljice Marije 16, 11000 Belgrade, Serbia*
[3] *Department for Production Engineering, Faculty of Technical Science, University of Novi Sad, Trg Dositeja Obradovica 6, 21000 Novi Sad, Serbia*
[4] *Faculty of Technology and Metallurgy, University of Belgrade, Karnegijeva 4, 11000 Belgrade, Serbia*

http://doi.org/10.5755/j02.ms.37307

*Received 16 May 2024; accepted 4 July 2024*

In this work, the morphology of the cavitation damage to centrifugally cast austenitic stainless alloys of the HP type was investigated. All specimens subjected to cavitation underwent detailed morphological analyses using light microscopy (LM) and scanning electron microscopy (SEM). The phase composition and lattice parameter verification were further analyzed by energy-dispersive x-ray spectroscopy (EDS) and x-ray diffraction spectroscopy (XRD). The mechanical properties of the material were evaluated by using tensile test, impact test, and macro and micro hardness measurements. The initial results indicate that the material microstructure consists of an austenitic matrix, accompanied by a continuous network of primary eutectic carbides. These carbides come in two types: one with a high concentration of Nb (visible as bright particles) and the other rich in Cr (seen as dark particles). The carbides are of the MC type, where M represents Nb, and of the complex $M_7C_3$ type, where M stands for Cr, Ni, and Fe. Carbides located within the inter-dendritic boundaries exhibit either lamellar or skeleton-like structures. The cavitation resistance of the centrifugally cast heat-resistant alloy – HP40 Nb, is primarily influenced by the morphology of the carbides and the mechanical characteristics of the austenitic matrix.

*Keywords:* austenitic stainless steel, cavitation resistant, microstructure, austenitic matrix, carbide phases.

## 1. INTRODUCTION

The phenomenon of cavitation, which is characterized by the formation and subsequent collapse of vapor structures within a liquid, is a common occurrence in various components of hydraulic machinery [1, 2]. The emission of shock waves and microjets during the collapse of vapor structures can interact with nearby solid surfaces, potentially leading to material damage [3 – 6]. Despite comprehensive investigations carried out so far, the problem of estimating material degradation due to cavitation has not been completely resolved.

In previous studies, the cavitation resistance of conventional materials, such as ferrous alloys frequently used in the fabrication of hydraulic machinery parts, depends on their mechanical properties, (such as hardness and tensile strength), as well as their microstructure [7, 8]. Most researchers [9 – 12] have correlated the cavitation erosion resistance of materials with microstructure, hardness, work-hardening ability, superelasticity and superplasticity, strain- or stress-induced phase transformation, etc. The cavitation resistance of Fe-Cr-Ni-C alloys is influenced by a range of factors. Cuppari et al. [13] found that the addition of 1 wt.% Ni to Fe-Cr-C-Si alloys significantly improved cavitation erosion resistance, while higher Ni concentrations had a detrimental effect. Wujun et al. [14] found that the introduction of Fe and Mo can decrease this resistance, while Park et al. [15] observed that the resistance decreases with increasing Ni concentration but improves with increasing Mn concentration.

The literature review indicates that while there is considerable scientific research on stainless steels, there is a lack of studies on centrifugally cast Fe-Cr-Ni-C alloys [10, 12, 15].

Centrifugally cast austenitic stainless-steel alloys of the HP type are widely used in the petrochemical industry to manufacture reformer furnace tubes, for operating at temperatures higher than 1123 K. These alloys have replaced the traditional super-alloys with a substantial reduction of cost and have equivalent properties under conditions of creep, with excellent resistances to high-temperature corrosion and carburization [16]. The microstructure of the alloy is multiphase and it consists of the supersaturated solid solution γ-Fe-Cr-Ni, as well as of the chromium and niobium carbides (CrxCy and NbxCy) [16, 17]. Literature reports [13 – 18] establish that erosion behavior is significantly influenced by the morphology of carbides, specifically their type, shape, size, volume, and distribution. Cuppari and al. [13] concluded that the cavitation resistance of materials, specifically those with an austenitic matrix and carbides, is determined by the morphology of the carbides and the mechanical characteristics of the matrix phase. Their findings indicated

* Corresponding author. Tel.: +38162241977.
E-mail: *eric.o@mas.bg.ac.rs* (O. Eric Cekic)

that the initial attack occurred at the carbide phase in the chromium alloys (comprising 25 % chromium) that exhibited carbides with a coarse morphology ($M_7C_3$). On the other hand, in alloys containing 35 % chromium and exhibiting finer morphology carbides ($M_{23}C_6$), the initiation of damage occurs at the interface between the carbide and the matrix [13]. A review of the literature reveals that despite extensive scientific studies on vanadium carbide in ledeburitic Cr-V steels and high-speed steels, there has been no observed enhancement in their erosion resistance, even with their high hardness [19]. The study by Seetharamu et al. [20] has shown that fine carbides in a matrix of austenite and martensite were found to impart a considerable amount of erosion resistance to high chromium irons. Similarly, the study of Chauhan et al. [21] showed that the erosion resistance of cast 21-4-N (21 %Cr-4 %Ni-0.4%N) steel is better, compared to that of 13/4 (13 %Cr-4 %Ni) martensitic steel due to the distribution of hard carbides in the matrix of stabilized austenite. In the other study, Chauhan et al. [21, 22] further showed that the stabilized austenite matrix of hot rolled 21-4-N steel is less prone to erosion damages as compared to the as-cast microstructure of 21-4-N and to stressed and untempered martensitic matrix of 13/4 steel, due to strain hardening. Gadhikar et al. [23] noted that in 23-8-N nitronic steel (composed of 23 % Cr, 8 % Ni, and 0.3 % N), the presence of carbides in band-like formations was found to increase the erosion rate. In contrast, larger carbides led to a reduction in carbon within the austenite matrix, negatively impacting the material's ability to harden under strain and subsequently reducing the erosion resistance of the overall material. However, they also observed that the erosion resistance of 23-8-N nitronic steel improved when carbides dissolved in the austenitic matrix following solution annealing [23].

The cavitation resistance of HP40 alloy in centrifugal casting was influenced by various parameters. Bampton et al. [24] found that damage, including cavitation porosity, in a superplastic aluminium alloy was dependent on the maximum principal stress. This suggests that stress-related factors, such as those controlled by centrifugal casting parameters, could affect cavitation resistance. The dominant production technology for HP40 tubes is centrifugal casting. The technological parameters such as mould material, mould rotation speed, casting temperature, chemical composition and casting dimension influence the product properties involved [25]. Espitia et al. [26] also highlight the role of microstructure and surface topography in cavitation resistance.

Therefore, in this paper the cavitation behavior of the heat-resistant centrifugal HP40 Nb alloy with respect to microstructural features was studied to confirm that this material can be used in conditions where cavitation erosion resistance is expected, considering the facts given above. The presented research aimed to establish the surface damage morphology of HP40 Nb alloy affected by cavitation.

## 2. MATERIALS AND METHODS

The chemical composition of the investigated alloy HP40 Nb in as-cast condition is given in Table 1. To establish the initial mechanical properties of the evaluated HP40 Nb alloys, tensile, hardness, and impact tests were performed. The tensile testing was performed according to ISO 6892-1 procedures on a hydraulic testing machine Schenk Hydropuls PSB250 (Darmstadt, Germany).

**Table 1.** Chemical composition of the HP40 Nb alloy (mass %)

| C | Mn | Si | P |
|---|---|---|---|
| 0.45 – 0.5 | max 1.5 | 1.5 – 2.0 | max 0.03 |
| Ni | Cr | Nb | Fe |
| 33.0 – 36.0 | 24.0 – 27.0 | 0.5 – 1.5 | balance |

Three specimens with a round cross-section, each having a gauge length of 30 mm and a diameter of 6 mm were used. The Vickers hardness measurement HV30 was conducted in compliance with ISO 6507 using a WEB HPO 250 machine (Leipzig, Germany), with a test load of 294.2 N (30 kgf) and a dwell time of 15 seconds. Additionally, the microhardness measurement HV0.1 was performed on a Wilson Tukon 1102 machine (Buehler, IL, USA) with a test load of 0.9807 N (0.1 kgf) and a dwell time of 15 seconds. The reported hardness value was the average of five measurements. The macro hardness HV30 included both the austenitic matrix and carbides, while the microhardness was measured between carbides to reduce their impact. The impact energy (KV2) was calculated for three samples as per the ISO 148-1 standard at room temperature using a TE Forcespeed Corporation JWT-450 machine (Jinan, China).

The standard procedure for preparing metallographic samples was employed before conducting a light microscopy examination. This process involved grinding with SiC papers (ranging from 180 to 2400), followed by polishing using diamond suspensions of varying particle sizes (6, 3, 1, and 1/4 μm). The sample was then etched with a solution composed of 15 ml HCl, 10 ml Glycerol, and 5 ml $HNO_3$.

Ultrasonic cavitation tests were done on a Branson Ultrasonics (Danbury, USA) JP40022A device, in accordance with the ASTM G32 standard [27]. The device operated at a vibration frequency of 20 ± 0.5 kHz and a peak-to-peak displacement amplitude of 50 μm. The specimens and the horn tip were separated by a distance of 0.5 mm. The tests were performed at a temperature of 25 ± 0.5 °C in water. The specimen had a diameter of 16 mm, a thickness of 6 mm, and a central aperture of 2 mm. The specimens were attached to the test rig using an 8 mm long screwed spigot. Before testing, the surfaces of the samples were prepared using metallography up to a 1 μm diamond paste. The mass loss of the test specimens was determined using an analytical balance with an accuracy of 0.1 mg, after the specimens were rinsed in alcohol and air-dried. Measurements were done at 15, 30, 45, and 60 minutes of cavitation exposure. Each reported mass loss point represents the average of three cavitation damage tests.

Microstructural and cavitated surfaces were observed by a Leitz Orthoplan light microscope (LM) from Wetzlar, Germany. Additionally, scanning electron microscopes (SEM) were used, specifically the JEOL JSM 6460LV (Tokyo, Japan), which is equipped with an EDS system INCA Oxford Instruments (High Wycombe, UK), and the JEOL JSM 5800, both operating at 20 kV.

## 3. RESULTS AND DISCUSSION

### 3.1. As-cast material

The LM and SEM micrographs of the alloy microstructure are given in Fig. 1a-b. The microstructure of HP40 Nb alloy at the initial state, in the as-cast condition, consists of an austenitic matrix and a skeletal-shaped primary eutectic carbides network. As can be seen, there are two types of morphologies for interdendritic eutectic-like primary carbides.

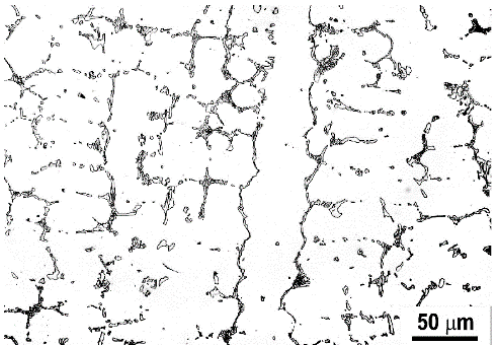


a

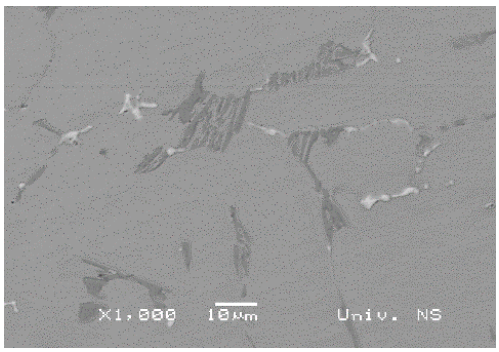


b

**Fig. 1.** The as-cast HP40 Nb alloy's microstructure is as follows: a – light microscopy (LM), 200×; b – scanning electron microscopy (SEM), 1000×

To investigate the intradendritic and interdendritic precipitates in as-cast HP40 Nb alloy, SEM observations were conducted in backscattered electron (BSE) mode with elemental mapping technique, Fig. 2. As illustrated in Fig. 1 b, and Fig. 2, two types of carbides could be distinguished, which exhibit darker and brighter contrast. In other words, the microstructure comprises an austenitic matrix (Spec. 5) and a continuous network of primary eutectic carbides. These carbides appeared in two varieties: one enriched with Nb (visible as bright particles in Fig. 2, Spec. 2 and Spec. 3) and the other enriched with Cr (visible as dark particles in Fig. 2, Spec. 1 and Spec. 4). These carbides are of the MC type, mainly NbC (bright), with additions of Cr, Fe, Ni, Ti; and of the $M_{23}C_6$ or/and $M_7C_3$ types, mainly Cr-C (dark grey), also with the addition of Fe and Ni.

Literature reveals that carbides, when present in the inter-dendritic boundaries, appear as lamellar or skeleton-form structures [28]. In addition, carbides with a high concentration of niobium have been found to maintain stability more effectively at elevated temperatures than secondary chromium carbides [29].

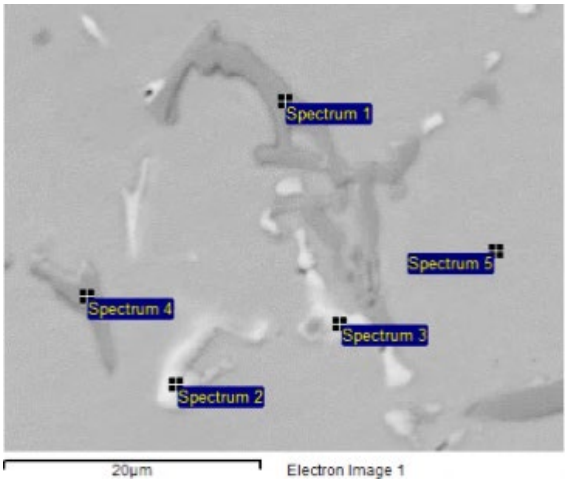


**Fig. 2.** SEM BSE micrograph of a cross-section of the HP40 Nb alloy – EDS point analysis

**Table 2.** The mass percentage of the chemical composition of the participate phases in the HP40 Nb alloy, corresponds to Fig. 2

| Specimen | C | Si | Ti | Cr | Mn | Fe | Ni | Nb |
|---|---|---|---|---|---|---|---|---|
| Spec. 1 | 37.04 | | | 54.19 | | 7.05 | 1.73 | |
| Spec. 2 | 43.00 | 0.98 | 0.60 | | | 9.47 | 8.45 | 27.41 |
| Spec. 3 | 43.60 | | 3.84 | 5.62 | | 3.45 | 2.71 | 40.78 |
| Spec. 4 | 17.04 | 2.52 | | 44.41 | | 19.40 | 16.64 | |
| Spec. 5 | 14.68 | 2.99 | | 22.29 | 0.97 | 30.75 | 28.32 | |

To further confirm the atomic structure of carbides, an XRD analysis is performed, Fig. 3. The lower section of Fig. 3 uses vertical lines to denote the reflection positions for the previously mentioned standard crystal types. These are derived from the PDF database and are accompanied by the numbers of their corresponding cards.

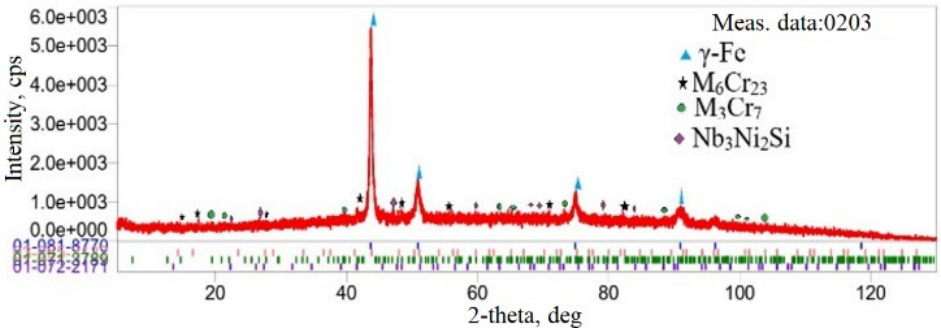


**Fig. 3.** The XRD patterns of the HP40 Nb alloy as cast are shown in red before cavitation

The initial row, highlighted in blue, signifies the reflection position of γ-Fe. The subsequent row, shown in pink, demonstrates the reflection position of $M_{23}C_6$. The tertiary row, indicated in green, exhibits the reflection positions of $M_7C_3$. Finally, the fourth row, highlighted in lilac, shows the reflection positions of $Nb_3Ni_2Si$.

In the HP40 Nb alloy sample, several crystal phases have been detected: γ-Fe, whose diffraction pattern, which aligns with the standard PDF # 01-081-8770, $Cr_{23}C_6$ that matches the standard PDF # 03-065-3132, $Cr_7C_3$ whose diffraction pattern corresponding to the standard PDF # 01-071-3789, and $Nb_3Ni_2Si$ that fits the standard PDF # 01-072-2171 (PDF-2 Release 2016 RDB).

The chemical analysis results suggest potential atomic substitutions in the aforementioned crystal structures.

This substitution includes the MC type (where M primarily represents Nb, supplemented by Cr, Fe, Ni, Ti), and the $M_{23}C_6$ or/and $M_7C_3$ types (where M primarily signifies Cr, supplemented by Fe and Ni). The provided crystal phase formulas should be viewed as approximate chemical formulas [28].

The starting mechanical properties of as-cast HP40 Nb alloy material are given in Table 3. The material has an average level of strength, lower hardness, and high brittleness compared to the other HP Nb alloys.

**Table 3.** Mechanical properties of the HP40 Nb alloy

| Material | $R_{p0.2}$, MPa | $R_m$, MPa | $A$, % | HV30 | Impact energy, J |
|---|---|---|---|---|---|
| HP40 Nb | 240 | 450 | 10 | 215 | 7.9 |

## 3.2. Cavitation damage of the material surface

### 3.2.1. Damage after 15 min

During the initial stages of cavitation testing, the austenite matrix, rather than the carbides, was the first to exhibit damage. As illustrated in Fig. 4, the austenite matrix, which is slightly attacked by the detachment of weakly bonded particles, is primarily where the damage unfolds. It could be assumed that this alteration is due to the disparity in hardness between the matrix and the carbides.

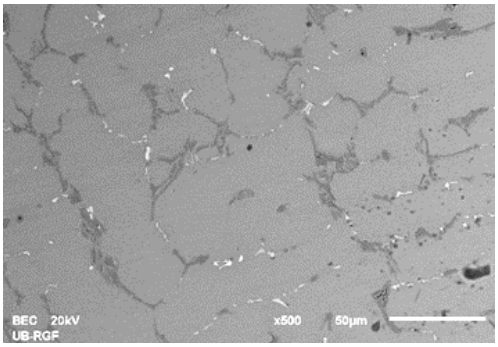


**Fig. 4.** SEM micrograph of HP40 Nb alloy after cavitation testing 15min

### 3.2.2. Damage after 30 min

After 30 minutes of cavitation testing, it might be noticed an increased extent of damage compared to the initial testing stage, as illustrated in Fig. 5 a. The carbides in some regions become partially fragmented (B – Fig. 5 b). At this stage, MC type Nb carbide becomes separated from the austenite matrix. Furthermore, it should be noted that the slip lines appear in austenite grains (C – Fig. 5 b). As shown in Fig. 5 c, the austenitic matrix, being softer than carbides, undergoes plastic deformation. The portion remaining after the carbides removal has the form of pits with notches with high-stress concentration and representing favorable locations for cavitation erosion. This finding is similar to the results of other researchers [10, 13, 14] who believed that the continuous effect of cavitation leads to material separation and pit formation. Plastic deformations occur in the austenitic matrix, i.e. the pushed-out part of the material appears near carbides.

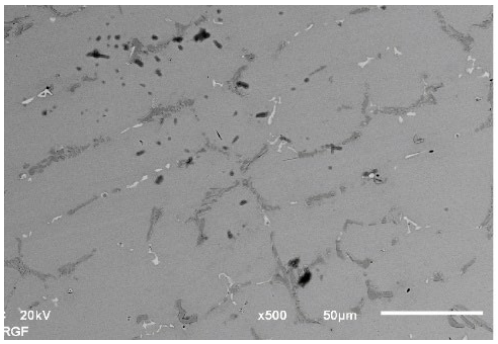


a

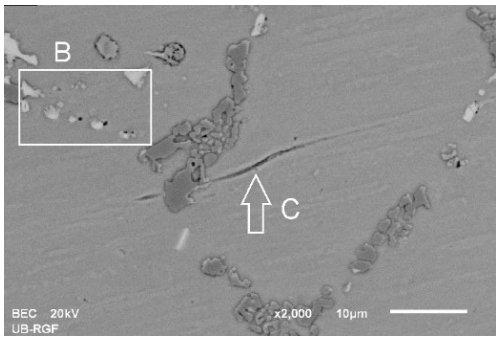


b

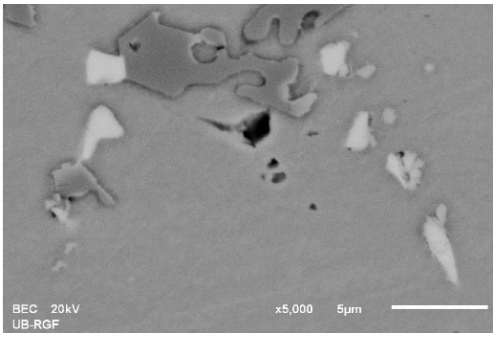


c

**Fig. 5.** SEM micrograph of cavitation damage after 30 min: a – the cavitated surface; b – B- the partially fragmented MC carbides of Nb, C-slip line; c – cavitation pit in the austenitic matrix

### 3.2.3. Cavitation damage after 60 min

Following 60 minutes of cavitation testing, one might notice further significant damage, as shown in Fig. 6. Surface deformations with an increasing number of cavities

and pitting were observed on the attacked areas of the specimen after 60 min of testing (Fig. 6). As the cavitation damage progresses, an increase in slip lines within the austenite grains can be observed. Material from these slip lines in the austenite grains is then eliminated by ductile fracture mode, as shown in Fig. 6 b. As the testing duration extended, cavitation caused the separation dislodgement of carbides, particularly primary ones, from the austenite matrix, resulting in the formation of new pits (Fig. 6 b and c). Higher magnification (Fig. 6 c) shows a characteristic detail where greater loss of metal, characterized by the removal of carbide phases with coarse morphology ($M_7C_3$), could be observed.

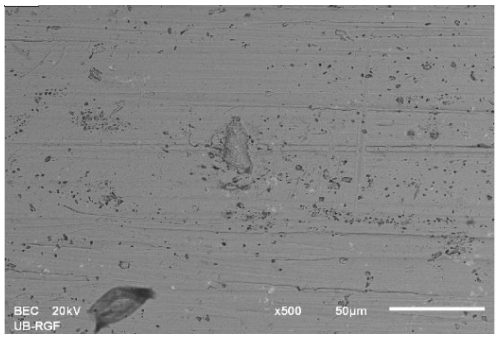


a

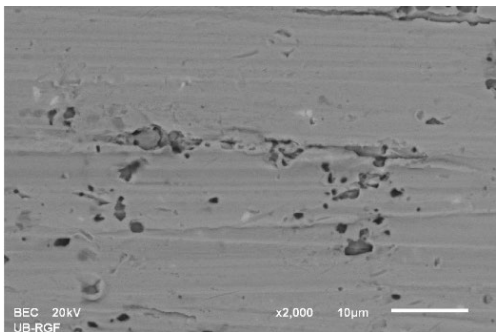


b

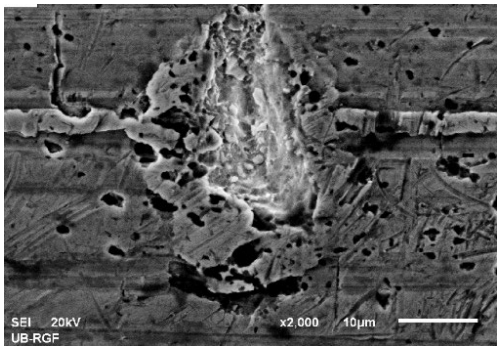


c

**Fig. 6.** SEM micrograph of cavitation damage after 60 min: a – surface overview; b – slip lines in austenite; c – removal of carbide phases

### 3.2.4. Cavitation erosion as a function of time

The diagram in Fig. 7 depicts the correlation between the loss of mass and cavitation duration. This relationship can be represented by a straight line, derived using the least-square method. The slope of the straight line represents the cavitation rate. The calculated slope for HP40 Nb alloy corresponds to the cavitation rate of 0.004 mg/min.

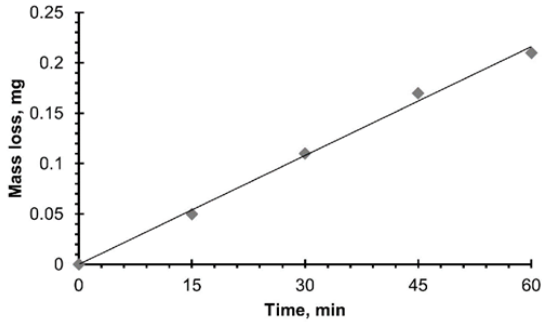


**Fig. 7.** Cavitation damage as a function of time

The results of the cavitation resistance examination of the test specimens are given in Fig. 7, which shows a linear relationship between the mass loss and testing time.

In summary, the initiation of cavitation damage in the HP40 Nb alloy occurs both at austenite grain boundaries and at the carbide-austenite interfaces [14]. In this type of alloy, $M_{23}C_6$ carbides have a finer morphology than that of $M_7C_3$ carbides. According to literary texts [13, 15], for alloys with finer carbides, the initiation of mass loss occurs at the interface between the carbide and the matrix.

Furthermore, also according to literature data [13] the coarser morphology of the $M_7C_3$ carbides is responsible for the increased mass loss of the alloys with 25 % chromium. The cavity surface is due to the dendritic casting microstructure, characterized by micro segregations of the alloying elements, which is consistent with the previous investigations about Fe-Cr-Ni based alloys [13, 14].

## 3.3. XRD analysis after cavitation

X-ray diffraction (XRD) patterns of the HP40 Nb alloy after cavitation are shown in Fig. 8.

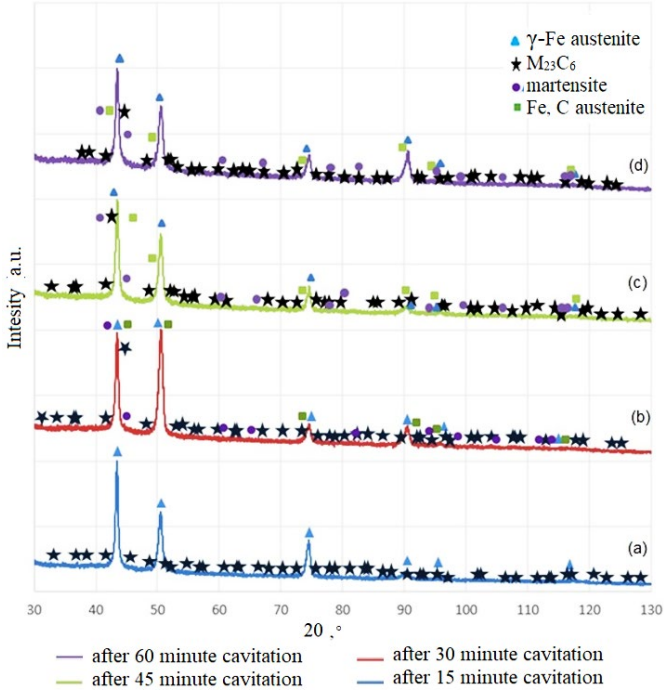


**Fig. 8.** XRD patterns for the HP40 Nb alloy after cavitation: a – 15 min; b – 30 min; c – 45 min; d – 60 min

The initial phase composition shows a precipitated carbide type $M_{23}C_6$ along with austenite. After 15 min of exposure to cavitation testing, the peaks at 2θ of 43.431(7)°, 50.514(10)°, 74.532(14)° correspond to (111), (200), (220) confirming the face-centred cubic (fcc) crystal austenite. Following a 30-minute cavitation test, α′-martensite was detected along with austenite and $M_{23}C_6$ carbide precipitates. After 30 min cavitation, the γ-peaks (representing austenite) decrease, indicating a transformation of the austenite into martensite.

With increasing time of cavitation, the change in the austenite amount is visible from the X-ray diffractogram. The peak intensities of the austenite (111γ and 200γ) are quite high during the first 15 min cavitation, while they are reduced after cavitation. This is because of the transformation of the face-centered cubic austenite to body-centered tetragonal martensite. It means that the formation α′ – martensite occurred in the already work-hardened austenite of this alloy.

Martensitic transformation significantly affects wear resistance and incubation time by steadily absorbing the cavity collapse energy.

According to Park et al. [34] in HP40 Nb alloy, an increase in the volume fraction of transformed α′-martensite during cavitation leads to an increase in the cavitation erosion resistance of Fe-Cr-Ni-C austenitic steel.

### 3.4. Microhardness changes

Fig. 9 shows the variation in microhardness in the cross-section of the examined HP40 Nb alloy before and after a cavitation test lasting between 15 and 60 minutes.

The variations of micro-hardness of the as-cast alloy (line 1#) and the alloy after 60 min cavitation process (line 2#) are shown in Fig. 9. For the as-cast alloy (line 1#), the micro-hardness is 219 HV0.1 and the value is lower compared to the surface hardness after 60 min cavitation process (line 2#). The Vickers micro-hardness (HV0.1) of the HP40 Nb alloy showed non-uniform values, and this is due to the difference in hardness between the austenite matrix and carbide particles.

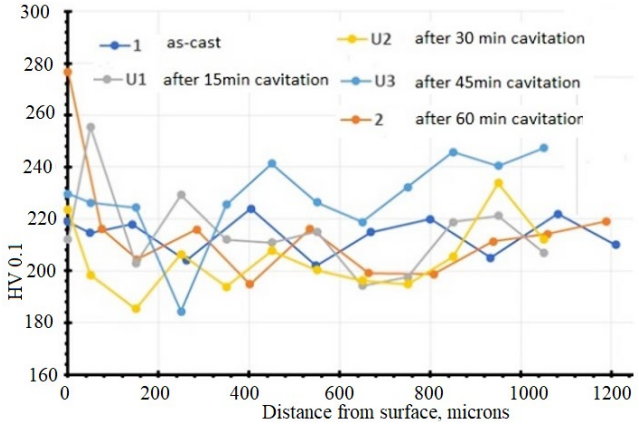


**Fig. 9.** Profile of microhardness vs. depth on a cross-section of the samples: 1 – as-cast; and U1 after 15 min, U2 after 30 min, U3 after 45 min; 2 – after 60 min cavitation damage

The Vickers micro-hardness (HV0.1) tests conducted on the cross-sections of the cavitated specimens are illustrated in Fig. 10.

In the area beneath the cavitated surface (up to 75 μm) a hardness increases to 277 HV0.1 is present for line 2#, in contrast to 219 HV0.1 for line 1# (in the as-cast state). The observed increase in micro-hardness verifies the previously mentioned XRD results of a transformation in the microstructure (formation of martensite) during cavitation, as well as the presence of work-hardened layers [30, 31]. This work hardening of the surface is due to microjets impacts during cavitation. The increase in microhardness with longer cavitation exposure time is observed. Based on the work hardening during cavitation, the microhardness increases as the cavitation exposure time lengthens, but it decreases due to peeling [30 – 33].

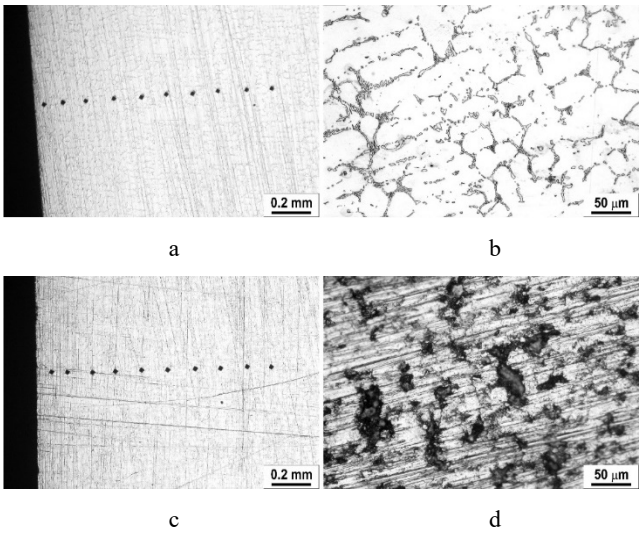


**Fig. 10.** LM cross-section and cavitated surface micrographs, respectively: a, b – as-cast condition, line 1#; c, d – after 60 min cavitation process, line 2#

The increase in microhardness with increased exposure time to cavitation of HP40 alloy can be attributed to several factors. Hu et al. [35] found that the size of craters and the thickness of the modified layer, both of which contribute to increased microhardness, increased with the number of high current pulsed electron beam (HCPEB) pulses. Similarly, Bai et al. [36] observed a significant improvement in microhardness at the end of the incubation period during ultrasonic cavitation peening. This suggests that prolonged exposure to cavitation can lead to increased microhardness. Additionally, the formation of extended graded structures and the non-uniform hardening of the alloy, as reported by Hu et al. [35], may also contribute to the increase in microhardness.

It is interesting to note that the level of the micro-hardness of as-cast alloy remained constant between 200 to 220 HV0.1.

## 5. CONCLUSIONS

According to the results obtained the following cavitation damage mechanism in centrifugally cast heat-resistant alloy – HP40 Nb could be established.

In the initial stage of testing, due to differences in the hardness of the matrix and carbide, the cavitation damage starts at the austenitic matrix (the austenitic matrix is softer than carbides). Primary eutectic carbides become separated

from the austenite matrix in the form of pits. During cavitation damage, slip lines form within the austenite grains. Material is subsequently removed from these slip lines in the austenite grains through a process known as ductile fracture. With the increased time of exposure to the effect of cavitation, damage develops along the grain boundaries. Followed by the destruction of the carbide types along the grain boundaries and the joining of the resulting holes and the formation of cracks.

It was determined on the cavitated sample cross-section that in the subsurface layer (up to 75 μm) the microhardness increases with time of exposure to cavitation, due to the work hardening effect induced by microjet impacts.

According to the obtained results, it can be summarized that the cavitation resistance primarily depends on the microstructure, corresponding hardness, and stress-induced phase transformation during cavitation.

## *Acknowledgments*

This work was supported by the Ministry of Science, Technological Development and Innovation of the Republic of Serbia, Contract No.: 451-03-65/2024-03/200135, Faculty of Technology and Metallurgy, University of Belgrade; 451-03-65/2024-03/200108, Faculty of Mechanical and Civil Engineering in Kraljevo, University of Kragujevac; 451-03-66/2024-03/ 200213, Innovation Centre of the Faculty of Mechanical Engineering, Belgrade, University of Belgrade; 451-03-65/2024-03/200156 and No. 01-3394/1 by Faculty of Technical Science, University of Novi Sad.

**REFERENCES**

1. **Knapp, R.T., Daily, J.W., Hammitt, F.G.** Cavitation, McGraw-Hill, New York, USA, 1970: pp. 578. https://www.amazon.com/Cavitation-Robert-T-Knapp/dp/0070350809
2. **Okada, T., Iwai, Y., Hattory, S., Tanimura, N.** Relation Between Impact Load and the Damage Produced by Cavitation Bubble Collapse *Wear* 184 (2) 1995: pp. 231 – 239. https://doi.org/10.1016/0043-1648(94)06581-0
3. **Hattori, S., Mori, H., Okada, T.** Quantitative Evaluation of Cavitation Erosion *Journal of Fluids Engineering* 120 (1) 1998: pp.179 – 185. https://doi.org/10.1115/1.2819644
4. **Hattori, S., Nakao, E.** Cavitation Erosion Mechanisms and Quantitative Evaluation Based on Erosion Particles Based on Erosion Particles *Wear* 249 (10 – 11) 2002: pp. 839 – 845. https://doi.org/10.1016/S0043-1648(00)00308-2
5. **Steller, J.** Cavitation Damage as a Result of Polyfractional Erosion Process *Wear* 456 – 457 2020: pp. 1 – 33. https://doi.org/10.1016/j.wear.2020.203369
6. **Dojčinović, M., Erić, O., Rajnović, D., Sidjanin, L., Baloš, S.** Effect of Austempering Temperature on Cavitation Behaviour of Unalloyed ADI Material *Materials Characterization* 82 (66) 2013: pp. 66 – 72. https://doi.org/10.1016/j.matchar.2013.05.005
7. **Szkodo, M.** Mathematical Description and Evaluation of Cavitation Erosion Resistance of Materials *Journal of Materials Processing Technology* 164 2005: pp. 1631 – 1636. https://doi.org/10.1016/j.jmatprotec.2005.01.006
8. **Hattori, S., Maeda, K., Zhang, Q.** Formulation of Cavitation Erosion Behavior Based on Logistic Analysis *Wear* 257 2004: pp. 10640 – 1070. https://doi.org/10.1016/j.wear.2004.07.009
9. **Liu, W., Zheng, Y.G., Yao, Z.M., WU, X.Q., Ke, W.** Cavitation Erosion of 20SiMn and 0Cr13Ni5Mo Steels in Distilled Water with and without Sand *Acta Metallurgica Sinica* 37 (2) 2001: pp. 197 – 201. https://doi.org/10.3321/j.issn:0412-1961.2001.02.018
10. **Heathcock, C.J., Protheroe, B.E., Ball, A.** Cavitation Erosion of Stainless Steels *Wear* 81 (2) 1982: pp. 311327. https://doi.org/10.1016/0043-1648(82)90278-2
11. **Cheng, F.T., Shi, P., Man, H.C.** Correlation of Cavitation Erosion Resistance with Indentation Derived Properties for a NiTi Alloy *Scripta Materialia* 45 2001: pp. 1083 – 1089. https://doi.org/10.1016/S1359-6462(01)01143-5
12. **Fu, W.T., Yang, Y.B., Jing, T.F., Zheng, Y.Z., Yao, M.** The Resistance to Cavitation Erosion of CrMnN Stainless Steels *Journal of Materials Engineering and Performance* 7 1998: pp. 801 – 804. https://link.springer.com/article/10.1361/105994998770347
13. **Cuppari, M.G., Di, V., Souza, R.M., Sinatora, A.** Effect of Hard Second Phase on Cavitation Erosion of Fe–Cr–Ni–C Alloys *Wear* 258 (1 – 4) 2005: pp. 596 – 603. https://doi.org/10.1016/j.wear.2004.09.019
14. **Wujun, Y., Di, F., Beijing, L., Heli, C.** Effect of Metallurgical Factors on the Resistance of Cavitation Erosion of Ni_3Al Based Alloys *Acta Metallurgica Sinica* 34 (11) 1998: pp. 1163 – 1166. https://www.ams.org.cn/EN/Y1998/V34/I11/1163
15. **Park, M.C., Kim, K.N., Shin, G.S., Yun, J.Y., Shin, M.H., Kim, S. J.** Effects of Ni and Mn on the Cavitation Erosion Resistance of Fe-Cr-C-Ni/Mn Austenitic Alloys *Tribology Letters* 52 2013: pp. 477 – 484. https://doi.org/10.1007/s11249-013-0231-x
16. **Cuppari, M.G.D.V., Wischnowski, F., Tanaka, D.K., Sinatora, A.** Correlation Between Microstructure and Cavitation–Erosion Resistance of High-Chromium Cast Steel—Preliminary Results *Wear* 225 – 229 1999: pp. 517 – 522. https://doi.org/10.1016/S0043-1648(98)00377-9
17. **Tancret, F., Laigo, J., Furtado, J.** Creep Resistance of Fe–Ni–Cr Heat Resistant Alloys for Reformer Tube Applications *Materials Science and Technology* 35(16) 2019: pp.1 – 8. https://doi.org/10.1080/02670836.2019.1648371
18. **Almeida, De L.H., Ribeiro, A.F., May, I.L.** Microstructural Characterization of Modified 25Cr–35Ni Centrifugally Cast Steel Furnace Tubes *Materials Characterization* 49 2003: pp. 219 – 229. https://doi.org/10.1016/S1044-5803(03)00013-5
19. **Liujie, X., Jiandong, X., Shizhong, W., Yongzhen, Z., Rui, L.** Investigation on Wear Behaviors of High-Vanadium High-Speed Steel Compared with High-Chromium Cast Iron Under Rolling Contact Condition *Materials Science and Engineering A* 434 2006: pp. 63 – 70. https://doi.org/10.1016/j.msea.2006.07.047
20. **Seetharamu, S., Sampathkumaran, P., Kumar, R.K.** Erosion Resistance of Permanent Moulded High Chromium Iron *Wear* 186 – 187 1995: pp. 159 – 167. https://doi.org/10.1016/0043-1648(95)07173-3
21. **Chauhan, A.K., Goel, D.B., Prakash, S.** Erosion Behaviour of Hydro Turbine Steels *Bulletin Materials Science* 31 (2) 2008: pp. 115 – 120. https://doi.org/10.1007/s12034-008-0020-6

22. **Chauhan, A.K., Goel, D.B., Prakash, S.** Solid Particle Erosion Behaviour of 13Cr–4Ni and 21Cr–4Ni–N Steels *Journal of Alloys and Compounds* 467 2009: pp. 459 – 464. https://doi.org/10.1016/j.jallcom.2007.12.053
23. **Gadhikar, A.A., Sharma, A., Goel, D.B., Sharma, C.P.** Effect of Carbides on Erosion Resistance of 23-8-N Steel *Bulletin of Materials Science* 37 (2) 2014: pp. 315 – 319. https://doi.org/10.1007/s12034-014-0656-3
24. **Bampton, C.C., Raj, R.** Influence of Hydrostatic Pressure and Multiaxial Straining on Cavitation in a Superplastic Aluminium Alloy *Acta Metallurgica* 30 1982: pp. 2043 – 2053. https://doi.org/10.1016/0001-6160(82)90107-9
25. **Wang, M.** Microstructure Characterisation and Creep Modelling of HP40 Alloy. School of Metallurgy and Materials, Springer, University of Birmingham, Birmingham, 2017: pp. 1 – 26. https://etheses.bham.ac.uk/id/eprint/7463/2/Wang17PhD
26. **Espitia, L.A., Toro, A.** Cavitation Resistance, Microstructure and Surface Topography of Materials Used for Hydraulic Components *Tribology International* 43 2010: pp. 2037 – 2045. https://doi.org/10.1016/J.TRIBOINT.2010.05.009
27. **ASTM G32-92:** Standard Method of Vibratory Cavitation Erosion Test 1992, ASTM International: West Conshohocken, PA. 2010 Retrieved from www.astm.org.
28. **Lee, J.H., Yang, W.J., Yoo, W.D., Cho, K.S.** Microstructural and Mechanical Property Changes in HK40 Reformer Tubes after Long Term Use *Engineering Failure Analysis* 16 2009: pp. 1883 – 1888. https://doi.org/10.1016/j.engfailanal.2008.09.032
29. **Timotijević, M., Erić Cekić, O., Rajnović, D., Dojčinović, M., Janjatović, P.** Microstructure Evolution and Mechanical Properties Degradation of HPNb Alloy after an Eleven-Year Service *Structural Integrity and Life* 22 (3) 2022: pp. 299 – 304. http://divk.inovacionicentar.rs/ivk/ivk22/299-IVK3-2022-MT-OEC-DR-MD-PJ.pdf
30. **Dojčinović, M., Volkov-Husović, T.** Cavitation Damage of the Medium Carbon Steel: Implementation of Image Analysis *Materials Letters* 62 2008: pp. 953 – 956. https://doi.org/10.1016/j.matlet.2007.07.019
31. **Karimi, A., Martin, J.L.** Cavitation Erosion of Materials *International Metals Reviews* 31 (1) 2013: pp. 1 – 26. https://doi.org/10.1179/imtr.1986.31.1.1
32. **Kumar, R.K., Kamaraj, M., Seetharamu, S., Pramod, T., Sampathkumaran, P.** Effect of Spray Particle Velocity on Cavitation Erosion Resistance Characteristics of HVOF and HVAF Processed 86WC-10Co4Cr Hydro Turbine Coatings *Journal of Thermal Spray Technology* 25 2016: pp. 1217 – 1230. https://doi.org/10.1007/s11666-016-0427-3
33. **Dojčinović, M., Marković, S.** The Morphology of Cavitation Damage of Heat-Treated Medium Carbon Steel *Journal of the Serbian Chemical Society – JSCS* 71 (8 – 9) 2006: pp. 977 – 984. https://doi.org/10.2298/JSC0609977D
34. **Park, M.C., Kim, K.N., Shin, G.S., Kim, S.J.** Effects of Strain Induced Martensitic Transformation on The Cavitation Erosion Resistance and Incubation Time of Fe–Cr–Ni–C alloys *Wear* 274 – 275 2012: pp. 28 – 33. https://doi.org/10.1016/j.wear.2011.08.011
35. **Hu, J.J., Zhang, G.B., Xu, H.B., Chen, Y.F.** Microstructure Characteristics and Properties of 40Cr Steel Treated by High Current Pulsed Electron Beam *Materials Technology* 27 (4) 2012: pp. 300 – 303. https://doi.org/10.1179/175355511X13171168481358
36. **Bai, F., Saalbach, K.A., Wang, L., Wang, X., Twiefel, J.** Impact of Time on Ultrasonic Cavitation Peening Via Detection of Surface Plastic Deformation *Ultrasonics* 84 2018: pp. 350 – 355. https://doi.org/10.1016/j.ultras.2017.12.001